Supplementary Material for Optimizing MR Scan Design for Model-Based T_1, T_2 Estimation from Steady-State Sequences

G. Nataraj[⋆], J. F. Nielsen[†], and J. A. Fessler[⋆]

[⋆]Dept. of Electrical Engineering and Computer Science, University of Michigan
[†]Dept. of Biomedical Engineering, University of Michigan

This supplement elaborates upon methodology details and presents additional figures that could not be included in the Manuscript [1] due to page restrictions. Section S.I provides visualizations of scan parameter optimization problem (9) in the Manuscript and relates min-max scan design to prior art. Section S.II describes methods for latent object parameter estimation from optimized scan profiles. Section S.III presents images and histograms corresponding to Manuscript Section IV.A. Section S.V elaborates upon image reconstruction and parameter estimation details for phantom and *in vivo* experiments (Manuscript Sections IV.B-IV.C). Lastly, Section S.VI explores the effect of model mismatch due to multi-exponential relaxation on single-component $\mathbf{T}_2$ estimation.

S.I Optimized Scan Design: Further Details

S.I.A Scan Profile Comparisons

Fig. S.1 displays heat maps of worst-case latent parameter standard deviations $\widetilde{\sigma}^{\mathrm{t}}_{T_1}$, $\widetilde{\sigma}^{\mathrm{t}}_{T_2}$ and worst-case cost $\widetilde{\Psi}^{\mathrm{t}}$ as pairs of flip angles are varied away from the optimized scan design $\mathbf{P}^*$. When present hereafter, boxes group subfigures corresponding to the same scan profile. Viewing the bottom row of subfigures, it is evident that $\widetilde{\Psi}^{\mathrm{t}}(\mathbf{P}^*)$ takes similar values for the different scan profiles. However, it is apparent that the $(C_{\mathrm{SPGR}}, C_{\mathrm{DESS}}) = (0, 2)$ profile is substantially more robust to flip angle variation than other tested profiles (namely, $(2, 1)$ and $(1, 1)$). Optimized worst-case cost over broadened latent parameter ranges $\widetilde{\Psi}^{\mathrm{b}}(\mathbf{P}^*)$ captures this by expanding the range of possible flip angles from $\mathcal{K}_{\mathrm{t}} = [0.9, 1.1]$ to $\mathcal{K}_{\mathrm{b}} = [0.5, 2]$ to account for factor-of-two spatial variation in relative flip angle $\boldsymbol{\kappa}$. As a result, we find that the properties of "broad" search criterion $\widetilde{\Psi}^{\mathrm{b}}(\cdot)$ provide a stronger reason to select the $(0, 2)$ scan for joint T_1, T_2 estimation in the brain than the properties of "tight" search criterion $\widetilde{\Psi}^{\mathrm{t}}(\cdot)$.

S.I.B Relation to Prior Art

To relate our work to other scan design methods, we apply min-max scan design to the well-studied problem of scan design for $\mathbf{T}_1$ estimation from two SPGR scans and compare our results with those of

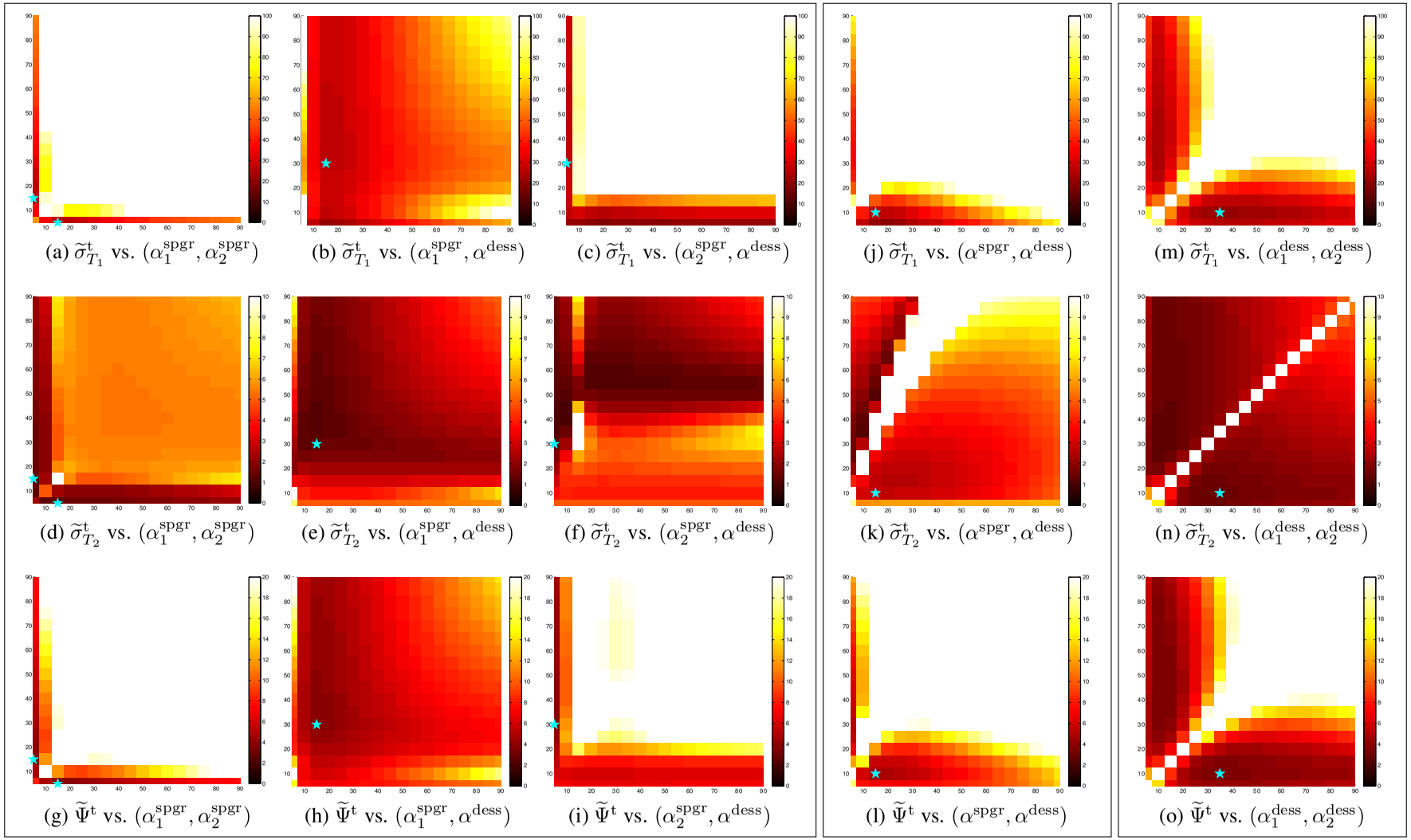

(a) $\widetilde{\sigma}^{\mathrm{t}}_{T_1}$ vs. $(\alpha_1^{\mathrm{spgr}}, \alpha_2^{\mathrm{spgr}})$ (b) $\widetilde{\sigma}^{\mathrm{t}}_{T_1}$ vs. $(\alpha_1^{\mathrm{spgr}}, \alpha^{\mathrm{dess}})$ (c) $\widetilde{\sigma}^{\mathrm{t}}_{T_1}$ vs. $(\alpha_2^{\mathrm{spgr}}, \alpha^{\mathrm{dess}})$ (j) $\widetilde{\sigma}^{\mathrm{t}}_{T_1}$ vs. $(\alpha^{\mathrm{spgr}}, \alpha^{\mathrm{dess}})$ (m) $\widetilde{\sigma}^{\mathrm{t}}_{T_1}$ vs. $(\alpha_1^{\mathrm{dess}}, \alpha_2^{\mathrm{dess}})$

(d) $\widetilde{\sigma}^{\mathrm{t}}_{T_2}$ vs. $(\alpha_1^{\mathrm{spgr}}, \alpha_2^{\mathrm{spgr}})$ (e) $\widetilde{\sigma}^{\mathrm{t}}_{T_2}$ vs. $(\alpha_1^{\mathrm{spgr}}, \alpha^{\mathrm{dess}})$ (f) $\widetilde{\sigma}^{\mathrm{t}}_{T_2}$ vs. $(\alpha_2^{\mathrm{spgr}}, \alpha^{\mathrm{dess}})$ (k) $\widetilde{\sigma}^{\mathrm{t}}_{T_2}$ vs. $(\alpha^{\mathrm{spgr}}, \alpha^{\mathrm{dess}})$ (n) $\widetilde{\sigma}^{\mathrm{t}}_{T_2}$ vs. $(\alpha_1^{\mathrm{dess}}, \alpha_2^{\mathrm{dess}})$

(g) $\widetilde{\Psi}^{\mathrm{t}}$ vs. $(\alpha_1^{\mathrm{spgr}}, \alpha_2^{\mathrm{spgr}})$ (h) $\widetilde{\Psi}^{\mathrm{t}}$ vs. $(\alpha_1^{\mathrm{spgr}}, \alpha^{\mathrm{dess}})$ (i) $\widetilde{\Psi}^{\mathrm{t}}$ vs. $(\alpha_2^{\mathrm{spgr}}, \alpha^{\mathrm{dess}})$ (l) $\widetilde{\Psi}^{\mathrm{t}}$ vs. $(\alpha^{\mathrm{spgr}}, \alpha^{\mathrm{dess}})$ (o) $\widetilde{\Psi}^{\mathrm{t}}$ vs. $(\alpha_1^{\mathrm{dess}}, \alpha_2^{\mathrm{dess}})$

Figure S.1: Worst-case standard deviations $\widetilde{\sigma}^{\mathrm{t}}_{T_1}$ (top), $\widetilde{\sigma}^{\mathrm{t}}_{T_2}$ (middle), and cost $\widetilde{\Psi}^{\mathrm{t}}$ (bottom), versus pairs of nominal flip angles, holding other scan parameters fixed at selected profile $\mathbf{P}^*$. Subfigures (a)-(i), (j)-(l), and (m)-(o) correspond to scan profiles containing $(C_{\mathrm{SPGR}}, C_{\mathrm{DESS}}) = (2,1), (1,1),$ and $(0,2)$ SPGR and DESS scans, respectively. Selected scan parameters (starred) are within $\delta = 1\%$ of global minimizers and retain as much estimator precision as possible over a wide range of latent object parameters. All axes range from 5 to 90 degrees, in 5-degree increments. Colorbar ranges are $[0, 100]$, $[0, 10]$, and $[0, 20]$ milliseconds for rows of $\widetilde{\sigma}^{\mathrm{t}}_{T_1}$, $\widetilde{\sigma}^{\mathrm{t}}_{T_2}$, and $\widetilde{\Psi}^{\mathrm{t}}$ subfigures, respectively. The optimized $(0,2)$ profile appears most robust to flip angle variation.

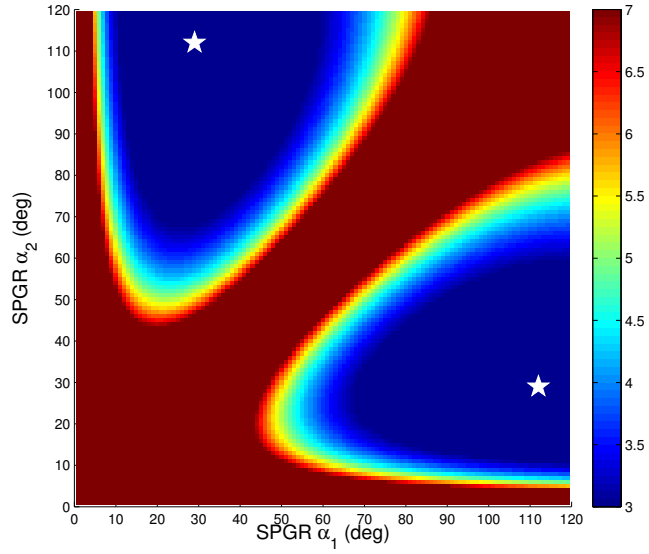

(a) $\widetilde{\sigma}^{\mathrm{t}}_{T_1}$ for nominal (T_1, κ), without $\mathbf{T}_{\mathrm{R}}$ optimization

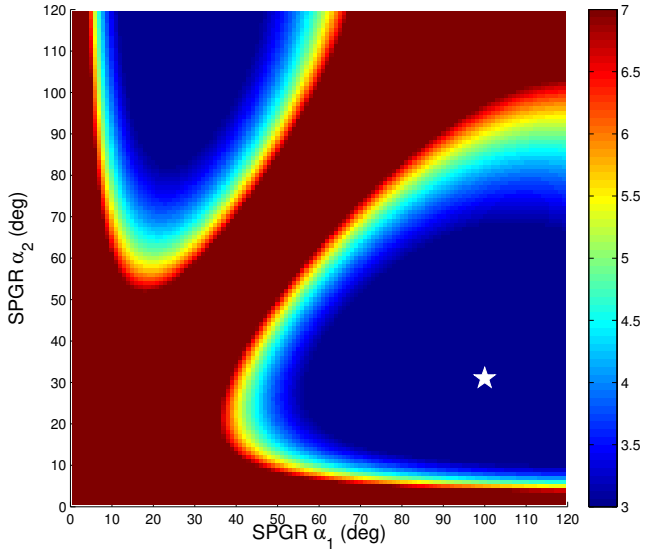

(b) $\widetilde{\sigma}^{\mathrm{t}}_{T_1}$ for nominal (T_1, κ), with $\mathbf{T}_{\mathrm{R}}$ optimization

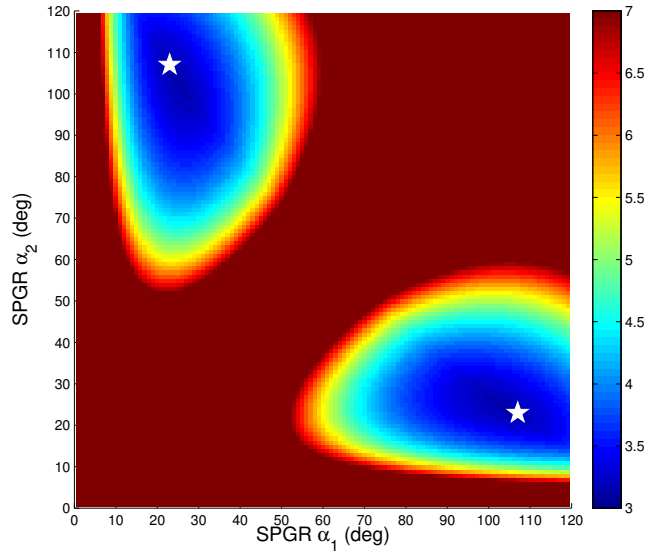

(c) $\widetilde{\sigma}^{\mathrm{t}}_{T_1}$ for GM/WM, without $\mathbf{T}_{\mathrm{R}}$ optimization

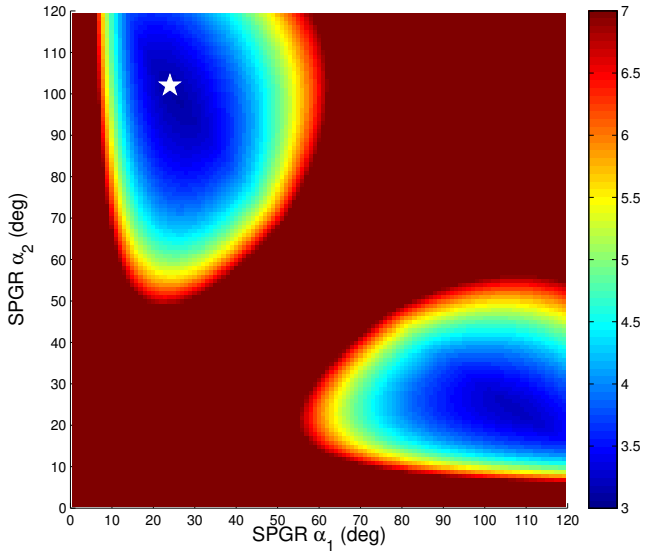

(d) $\widetilde{\sigma}^{\mathrm{t}}_{T_1}$ for GM/WM, with $\mathbf{T}_{\mathrm{R}}$ optimization

Figure S.2: Worst-case standard deviation $\widetilde{\sigma}^{\mathrm{t}}_{T_1}$ versus pairs of nominal SPGR flip angles, holding other scan parameters fixed at selected profile $\mathbf{P}^*$. Fig. S.2a (replicated from [2]) illustrates $\widetilde{\sigma}^{\mathrm{t}}_{T_1}$ (at single-point design ranges $\mathcal{X}_{\mathrm{t}} := \mathcal{M}_{\mathrm{E,t}} \times \mathcal{T}_{1,\mathrm{t}} \leftarrow (1, 1000\mathrm{ms})$ and $\mathcal{N}_{\mathrm{t}} := \mathcal{K} \leftarrow 1$) as flip angles are varied but $\mathbf{T}_{\mathrm{R}} \leftarrow [800, 800]^{\mathsf{T}}\mathrm{ms}$ remains fixed. Fig. S.2b (related to [3]) shows that lower $\widetilde{\sigma}^{\mathrm{t}}_{T_1}$ is achievable by allowing $\mathbf{T}_{\mathrm{R}}$ to vary as well. Figs. S.2c and S.2d illustrate how corresponding optimized designs change when $\widetilde{\sigma}^{\mathrm{t}}_{T_1}$ is instead evaluated over GM/WM ROIs $\mathcal{X}_{\mathrm{t}} \leftarrow 1 \times [800, 1400]\,\mathrm{ms}$ and $\mathcal{K}_{\mathrm{t}} \leftarrow [0.9, 1.1]$. Selected scan parameters (starred) are within $\delta = 1\%$ of global minimizers. Colorbar ranges are in milliseconds.

[2, 3]. We study [2, 3] over other works [4–6] because our purpose here is to demonstrate the utility of considering a range of design parameters, perhaps through our min-max formulation. The methods of [2, 3] are amenable to this purpose, as they study special cases of min-max optimization problem (6) in which the object parameter space $\mathcal{X}_{\mathrm{t}} \times \mathcal{N}_{\mathrm{t}}$ is a single point.

Subfigure [Method]	S.2a [2]	S.2b [3]	S.2c [1]	S.2d [1]
$\mathcal{T}_{1,\mathrm{t}}$	1000ms	1000ms	$[800, 1400]$ms	$[800, 1400]$ms
$\mathcal{K}_{\mathrm{t}}$	1	1	$[0.9, 1.1]$	$[0.9, 1.1]$
$\mathcal{T}_{\mathrm{R,SPGR}}$	$[800, \infty)$ms	$[12.2, \infty)$ms	$[800, \infty)$ms	$[12.2, \infty)$ms
$\mathcal{A}_{0,\mathrm{SPGR}}$	$[1, 120]^\circ$	$[1, 120]^\circ$	$[1, 120]^\circ$	$[1, 120]^\circ$
$T_{\mathrm{R,max}}$	1600ms	1600ms	1600ms	1600ms
$\widehat{\alpha}_0^{\mathrm{spgr}}$	$(29, 112)^\circ$	$(31, 100)^\circ$	$(23, 107)^\circ$	$(24, 102)^\circ$
$\widehat{T}_R^{\mathrm{spgr}}$	$(800, 800)$ms	$(1010, 590)$ms	$(800, 800)$ms	$(870, 730)$ms
$\widetilde{\sigma}^{\mathrm{t}}_{T_1}(\mathbf{P}^*)$, single-pt $\mathcal{X}_{\mathrm{t}} \times \mathcal{N}_{\mathrm{t}}$	1.97ms	1.89ms	2.04ms	1.99ms
$\widetilde{\sigma}^{\mathrm{t}}_{T_1}(\mathbf{P}^*)$, WM/GM $\mathcal{X}_{\mathrm{t}} \times \mathcal{N}_{\mathrm{t}}$	3.47ms	3.41ms	**3.18**ms	**3.13**ms
Run Time	6s	5m11s	2m29s	2h5m13s

Table S.1: Description and performance summary of four methods for optimization of two SPGR scans for precise T_1 estimation. Columns correspond with subfigures of Fig. S.2. Column 2 replicates results given in [2], which optimizes $\boldsymbol{\alpha}$ at fixed $\mathbf{T}_{\mathrm{R}}$ and nominal $\mathbf{x}, \boldsymbol{\nu}$ values. Column 3 uses ideas presented in [3] to improve [2] by optimizing both $\boldsymbol{\alpha}$ and $\mathbf{T}_{\mathrm{R}}$, under a time constraint. Columns 4-5 repeat the experiments of Columns 2-3, but over $\mathcal{X}_{\mathrm{t}} \times \mathcal{N}_{\mathrm{t}}$ corresponding to WM/GM at 3T.

Table S.1 summarizes how, with appropriate choices of parameter spaces, weights, and constraints, previous methods relate to min-max scan design (corresponding illustrations provided in Fig. S.2). To assess the utility of min-max design, we compare worst-case standard deviation $\widetilde{\sigma}^{\mathrm{t}}_{T_1}$ (computed with unity M_0 and constant noise variance $\sigma^2 \leftarrow 1.49 \times 10^{-7}$ as in the Manuscript) over the same WM/GM parameter space $\mathcal{X}_{\mathrm{t}} \times \mathcal{N}_{\mathrm{t}}$. Comparing Columns 2 and 4, we observe an 8.7% reduction in WM/GM $\widetilde{\sigma}^{\mathrm{t}}_{T_1}$ through min-max consideration for flip angle optimization. Similarly comparing columns 3 and 5, we observe an 8.6% reduction in WM/GM $\widetilde{\sigma}^{\mathrm{t}}_{T_1}$ through min-max consideration for flip angle and repetition time optimization. Each min-max grid-search takes roughly $25\times$ longer than its min-only counterpart. This substantial increase in (offline) computation time could likely be reduced through gradient-based optimization, at the expense of forgoing global for instead local optima.

S.II Latent Object Parameter Estimation from Optimized Scan Profiles

To experimentally validate scan designs, we require a method to obtain parameter estimates from data collected using the optimized scan parameters $\mathbf{P}^*$. Here, we describe maximum-likelihood (ML) and regularized least-squares (RLS) optimization approaches for latent object parameter estimation.

When the reconstructed images have V voxels centered at positions $\mathbf{r}_1, \ldots, \mathbf{r}_V$, an ML estimator $\widehat{\mathbf{X}}_{\mathrm{ML}}(\mathbf{N}, \mathbf{P}^*)$ minimizes over $\mathbf{X}$ the negative log-likelihood

$$\Psi^{\mathrm{ML}}(\mathbf{X}; \mathbf{N}, \mathbf{P}^*) = \frac{1}{2} \left\| \Sigma^{-1/2} \left(\mathbf{Y} - \mathbf{F}(\mathbf{X}; \mathbf{N}, \mathbf{P}^*) \right) \right\|_F^2, \tag{S.1}$$

where matrices $\mathbf{Y} := [\mathbf{y}(\mathbf{r}_1), \ldots, \mathbf{y}(\mathbf{r}_V)] \in \mathbb{C}^{D \times V}$, $\mathbf{X} := [\mathbf{x}(\mathbf{r}_1), \ldots, \mathbf{x}(\mathbf{r}_V)] \in \mathbb{C}^{L \times V}$, and $\mathbf{N} := [\boldsymbol{\nu}(\mathbf{r}_1), \ldots, \boldsymbol{\nu}(\mathbf{r}_V)] \in \mathbb{C}^{K \times V}$ are discretizations over V voxel locations of vector counterparts; matrix function $\mathbf{F} : \mathbb{C}^{L \times V} \times \mathbb{C}^{K \times V} \times \mathbb{C}^{P \times D} \mapsto \mathbb{C}^{D \times V}$ naturally extends $\mathbf{f}$; $\mathbf{P}^*$ remains the optimized scan profile from (9); and $\|\cdot\|_F$ denotes the Frobenius norm.

Often, it is reasonable to assume that each latent object parameter map is (possibly piecewise) smooth. To exploit this prior knowledge, we estimate $\mathbf{X}$ by minimizing over search space $\mathcal{X}^V$ an extension of (S.1) that includes regularization:

$$\widehat{\mathbf{X}}_{\mathrm{RLS}}\left(\mathbf{N}, \mathbf{P}^*\right) \in \underset{\mathbf{X} \in \mathcal{X}^V}{\arg\min}\, \Psi^{\mathrm{RLS}}(\mathbf{X}; \mathbf{N}, \mathbf{P}^*), \quad \text{where} \tag{S.2}$$

$$\Psi^{\mathrm{RLS}}(\mathbf{X}; \mathbf{N}, \mathbf{P}^*) = \Psi^{\mathrm{ML}}(\mathbf{X}; \mathbf{N}, \mathbf{P}^*) + \sum_{l=1}^{L} R_l([\mathbf{X}]_l^{\mathsf{T}}) \tag{S.3}$$

and $[\cdot]_r$ extracts the rth row of its argument. Here, we have introduced regularizer functions $R_l(\cdot) : \mathbb{C}^V \mapsto \mathbb{R}$ for $l \in \{1, \ldots, L\}$, which in this work are chosen as

$$R_l(\cdot) := \beta_l \sum_{j=1}^{J} \phi_l \left(\left[\mathbf{C}(\cdot) \right]_j \right), \tag{S.4}$$

where β_l is a regularization parameter; $\phi_l : \mathbb{C} \mapsto \mathbb{R}$ is a (possibly edge-preserving) convex penalty function, selected based on expected properties of the lth latent object parameter; $\mathbf{C} \in \mathbb{R}^{J \times V}$ is a finite differencing matrix; and j indexes a total J direction-dependent differencing operations.

Typically, $\Psi^{\mathrm{RLS}}(\mathbf{X}; \mathbf{N}, \mathbf{P}^*)$ is non-convex in $\mathbf{X}$, precluding global optimization. We instead seek a local minimizer of (S.3) using the projected Levenberg-Marquardt method [7] with a step-halving line search to ensure monotonic convergence in cost.

For non-convex cost functions like (S.3), initialization quality is important. In this work, we initialize (S.2) by first isolating nonlinear dependencies via the "variable-projection" method [8], and then minimizing (S.1) using a nonlinear least-squares (NLS) algorithm. Specifically, we note that $\Psi^{\mathrm{ML}}(\mathbf{X}; \mathbf{N}, \mathbf{P}^*)$ is voxel-wise separable, and thereby find a global minimizer of (S.1) in a single iteration of matching pursuit [9, 10] with a precomputed dictionary of signal vectors.

Following an analysis similar to that of [11] for the NLS objective (S.1), one can show that if $\mathbf{f}$ is a smooth, injective mapping and dictionary quantization error is neglected, then $\widehat{\mathbf{X}}_{\mathrm{ML}}(\mathbf{N}, \mathbf{P}^*)$ is asymptotically efficient. At reasonable noise levels, we thus expect $\mathbf{P}^*$ to permit low ML estimation variance. For suitable regularizers, minimizing (S.3) with initialization $\widehat{\mathbf{X}}_{\mathrm{ML}}(\mathbf{N}, \mathbf{P}^*)$ then only further reduces variance.

Even for nonlinear $\mathbf{f}(\cdot)$, the ML estimate $\widehat{\mathbf{X}}_{\mathrm{ML}}$ is asymptotically unbiased. For Gaussian noise models, increasing sample size is statistically equivalent to increasing signal-to-noise ratio (SNR). Thus, in regions where the data provides sufficiently high SNR (and is thus approximately Gaussian-distributed even in magnitude [12]), $\widehat{\mathbf{X}}_{\mathrm{ML}}$ will exhibit negligible bias, and the CRB can be used to reliably predict ML estimation error. Table II in Section IV empirically explores the validity of this high-SNR assumption, through simulations at realistic noise levels.

S.III Numerical Simulations

Fig. S.3 displays latent object parameter estimates $\widehat{\mathbf{T}}_1^{\mathrm{ML}}$ and $\widehat{\mathbf{T}}_2^{\mathrm{ML}}$ from the optimized scan profiles alongside ($5\times$ magnified) absolute differences with respect to the ground truth (corresponding sample statistics within WM/GM regions of interest are summarized in Table II). Difference images suggest that, with careful scan optimization, all three scan profiles permit $\mathbf{T}_1$ and $\mathbf{T}_2$ to be jointly estimated with low error.

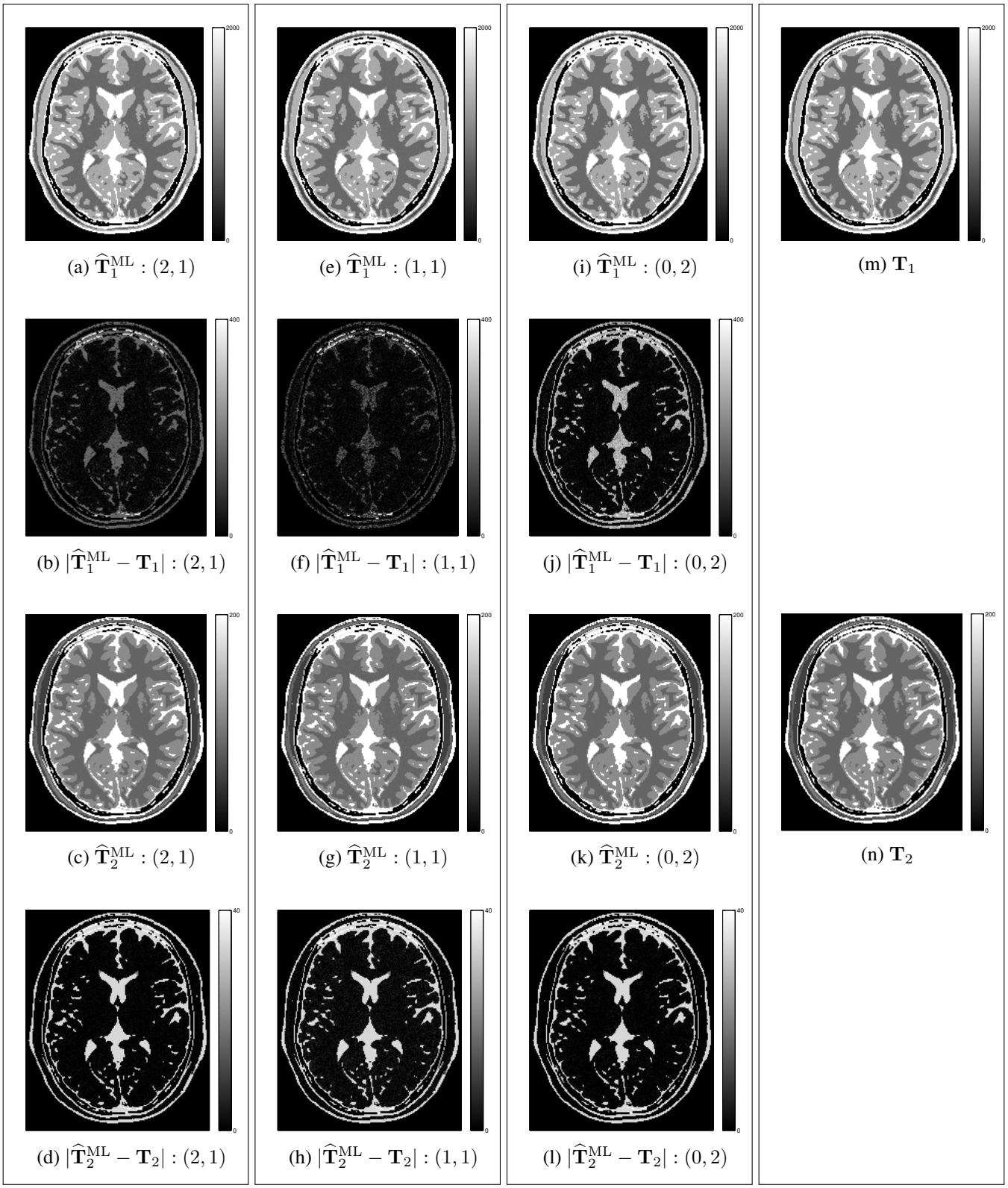

(a) $\widehat{\mathbf{T}}_1^{\mathrm{ML}} : (2,1)$ (e) $\widehat{\mathbf{T}}_1^{\mathrm{ML}} : (1,1)$ (i) $\widehat{\mathbf{T}}_1^{\mathrm{ML}} : (0,2)$ (m) $\mathbf{T}_1$

(b) $|\widehat{\mathbf{T}}_1^{\mathrm{ML}} - \mathbf{T}_1| : (2,1)$ (f) $|\widehat{\mathbf{T}}_1^{\mathrm{ML}} - \mathbf{T}_1| : (1,1)$ (j) $|\widehat{\mathbf{T}}_1^{\mathrm{ML}} - \mathbf{T}_1| : (0,2)$

(c) $\widehat{\mathbf{T}}_2^{\mathrm{ML}} : (2,1)$ (g) $\widehat{\mathbf{T}}_2^{\mathrm{ML}} : (1,1)$ (k) $\widehat{\mathbf{T}}_2^{\mathrm{ML}} : (0,2)$ (n) $\mathbf{T}_2$

(d) $|\widehat{\mathbf{T}}_2^{\mathrm{ML}} - \mathbf{T}_2| : (2,1)$ (h) $|\widehat{\mathbf{T}}_2^{\mathrm{ML}} - \mathbf{T}_2| : (1,1)$ (l) $|\widehat{\mathbf{T}}_2^{\mathrm{ML}} - \mathbf{T}_2| : (0,2)$

Figure S.3: $\mathbf{T}_1$ and $\mathbf{T}_2$ ML estimates and corresponding errors, from data synthesized using the optimized scan profiles in Table I. Subfigures (a)-(d), (e)-(h), and (i)-(l) correspond to scan profiles $(C_{\mathrm{SPGR}}, C_{\mathrm{DESS}}) = (2,1), (1,1),$ and $(0,2)$ SPGR and DESS scans, respectively. Colorbar ranges corresponding to $\mathbf{T}_1^{\mathrm{ML}}$ and $\mathbf{T}_2^{\mathrm{ML}}$ estimates are $[0, 2000]$ms and $[0, 200]$ms, respectively. Magnitude error maps are computed with respect to latent, ground truth (m) $\mathbf{T}_1$ and (n) $\mathbf{T}_2$ maps, and are respectively presented with $5\times$ magnified colorbar ranges $[0, 400]$ms and $[0, 40]$ms to aid comparison.

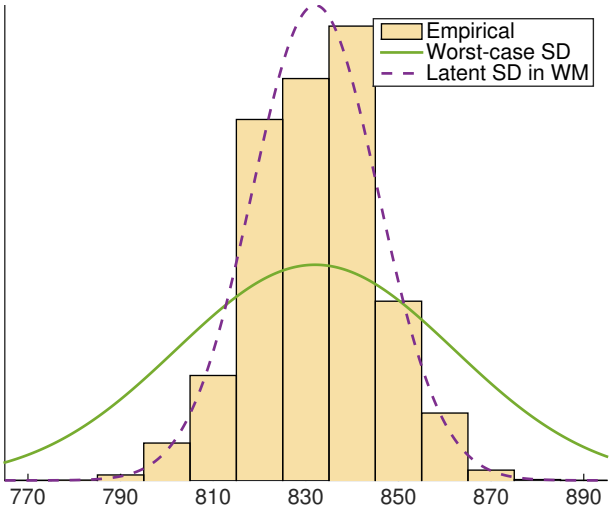

(a) $\widehat{T}_1^{\mathrm{ML}}$ (ms) in voxels with true WM-like $T_1 \leftarrow 832$

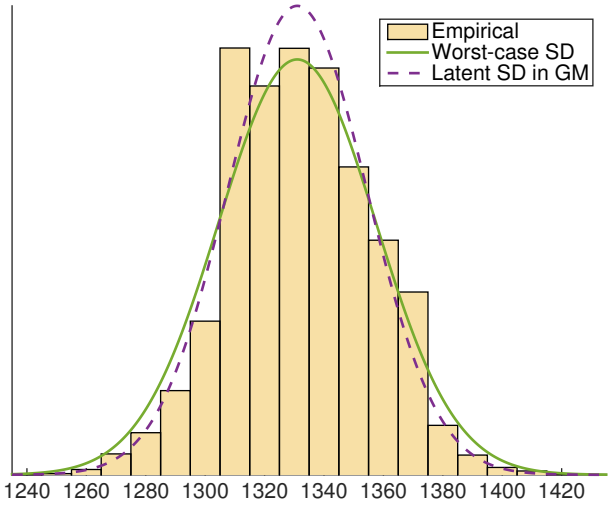

(b) $\widehat{T}_1^{\mathrm{ML}}$ (ms) in voxels with true GM-like $T_1 \leftarrow 1331$

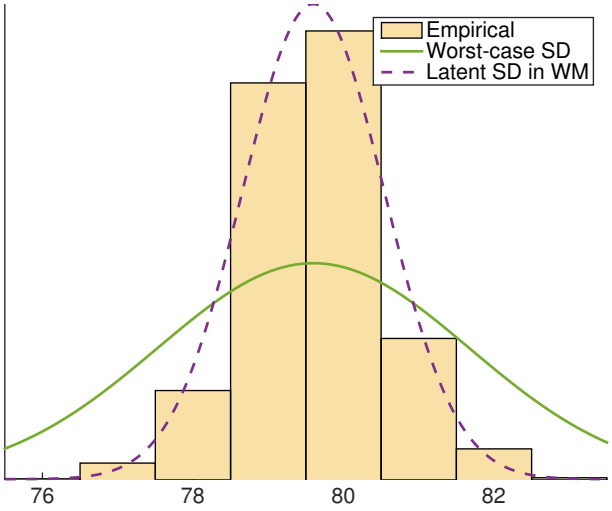

(c) $\widehat{T}_2^{\mathrm{ML}}$ (ms) in voxels with true WM-like $T_2 \leftarrow 79.6$

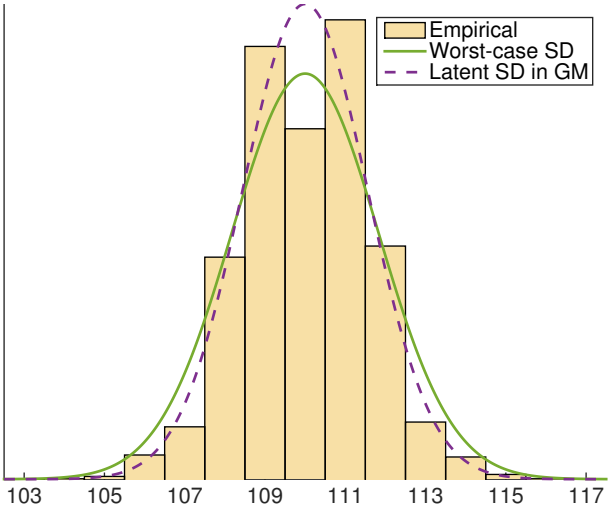

(d) $\widehat{T}_2^{\mathrm{ML}}$ (ms) in voxels with true GM-like $T_2 \leftarrow 110$

Figure S.4: Histograms of T_1 and T_2 estimates from noisy independent measurements of a *single* nominal WM or GM value. In each plot, two normal distributions are overlaid, each with latent means T_1 and T_2. In (a)-(b) and (c)-(d), the solid green curve is $\mathcal{N}(T_1, (\widetilde{\sigma}_{T_1}^{\mathrm{t}})^2)$ and $\mathcal{N}(T_2, (\widetilde{\sigma}_{T_2}^{\mathrm{t}})^2)$, respectively. In (a)-(d), the dashed maroon curves have variances computed from the Fisher information at *a priori* unknown T_1, T_2 values in WM or GM. These plots correspond to an optimized $(0, 2)$ scan profile; analogous plots for other profiles are visually similar. At realistic noise levels, parameter estimates distribute with minimal bias and near-Gaussian shape. Thus, the CRB can be used to reliably approximate $\widehat{T}_1^{\mathrm{ML}}$ and $\widehat{T}_2^{\mathrm{ML}}$ errors.

Fig. S.4 histograms (voxel-wise independent) ML estimates $\widehat{T}_1^{\mathrm{ML}}$ and $\widehat{T}_2^{\mathrm{ML}}$ from the $(0, 2)$ scan profile. Each histogram is over a WM or GM ROI, within which all voxels are assigned the same single-component true T_1 and T_2 nominal value, listed in Table II.

Overlaid in dashed maroon are normal distributions with latent means T_1 and T_2 and variances computed from the Fisher matrix at T_1, T_2 values in WM or GM. It is apparent that despite finite SNR and Rician noise, $\widehat{T}_1^{\mathrm{ML}}$ and $\widehat{T}_2^{\mathrm{ML}}$ exhibit negligible bias and near-Gaussian shape, suggesting locally linear behavior of the DESS signal model in T_1 and T_2 ($\widehat{T}_1^{\mathrm{ML}}$ and $\widehat{T}_2^{\mathrm{ML}}$ distributions from other profiles are similar).

The subfigures of Fig. S.4 superimpose in solid green a second set of normal distributions, with the same means T_1 and T_2 as before, but worst-case standard deviations $\widetilde{\sigma}_{T_1}^{\mathrm{t}}$ and $\widetilde{\sigma}_{T_2}^{\mathrm{t}}$. The separations between these distribution pairs visually depict how estimator variances specific to WM or GM T_1 and T_2 values differ from worst-case variances. Using the fixed latent object parameters to optimize scan profiles can tailor scans for precise estimation in *either* WM *or* GM. In contrast, the proposed min-max formulation finds scan parameters that ensure precise estimation in *both* WM *and* GM.

S.IV Flip Angle Scaling Calibration

In initial experiments, we found that even small (*e.g.*, $\sim$5%) modifications of flip angle scaling estimate $\widehat{\boldsymbol{\kappa}}$ from Bloch-Siegert (BS) shifted SPGR scans resulted in significant (*e.g.*, $\sim$10-15%) changes in SPGR/DESS $\widehat{\mathbf{T}}_1$ estimates. Here, we investigate possible $\widehat{\boldsymbol{\kappa}}$ estimation bias by comparing (via a separate study) $\widehat{\boldsymbol{\kappa}}$ from Bloch-Siegert (BS) [13] versus reference Double Angle (DA) [14] measurements.

We collect 8-channel BS and DA data in a structureless FIRST-BIRN gel phantom [15] ($T_1 \approx 520$ms via separate IR measurements). For DA (SPGR) scans, we prescribe nominal flip angles $\widehat{\boldsymbol{\alpha}}_0 \leftarrow [45^\circ, 90^\circ]^{\mathsf{T}}$ and long repetition times $\mathbf{T}_{\mathrm{R}} \leftarrow [3200, 3200]^{\mathsf{T}}$ms. Except for a reduced $256 \times 256 \times 6$ matrix, all other BS and SPGR acquisition details are the same as in Section IV.B.1.

We separately normalize and combine (via an extension of [16]) each pair of BS and DA coil datasets. To reduce errors due to $\mathbf{k}$-space truncation in regularized $\boldsymbol{\kappa}$ estimates, we mask out coil-combined image voxels outside and very near the phantom encasing. Initializing with respective method-of-moments estimates, we apply the methods of [17] and [18] to produce regularized $\boldsymbol{\kappa}$ estimates from coil-combined BS versus DA images.

Fig. S.5 reveals that well inside the phantom, BS and DA $\boldsymbol{\kappa}$ estimates exhibit paraboloidal spatial profiles (as expected), but differ in scaling. Specifically, within a centered ROI of 6758 voxels, the ratio of RLS DA $\widehat{\boldsymbol{\kappa}}$ to RLS BS $\widehat{\boldsymbol{\kappa}}$ has ROI sample mean $\pm$ ROI sample standard deviation of 1.050 ± 0.0044.

To reduce error propagation due to $\widehat{\boldsymbol{\kappa}}$ bias but retain the speed of BS acquisitions, we choose to scale up BS $\boldsymbol{\kappa}$ estimates in all phantom and *in vivo* experiments by 5.0%. We find empirically that even this crude correction factor greatly improves $\widehat{\mathbf{T}}_1$ agreement across SPGR/DESS and reference IR/SE scan profiles.

S.V Experimental Details

This section provides further details on phantom and *in vivo* experiments discussed in Sections IV.B and IV.C. Sections S.V.A and S.V.B provide phantom reconstruction details about SPGR/DESS and IR/SE

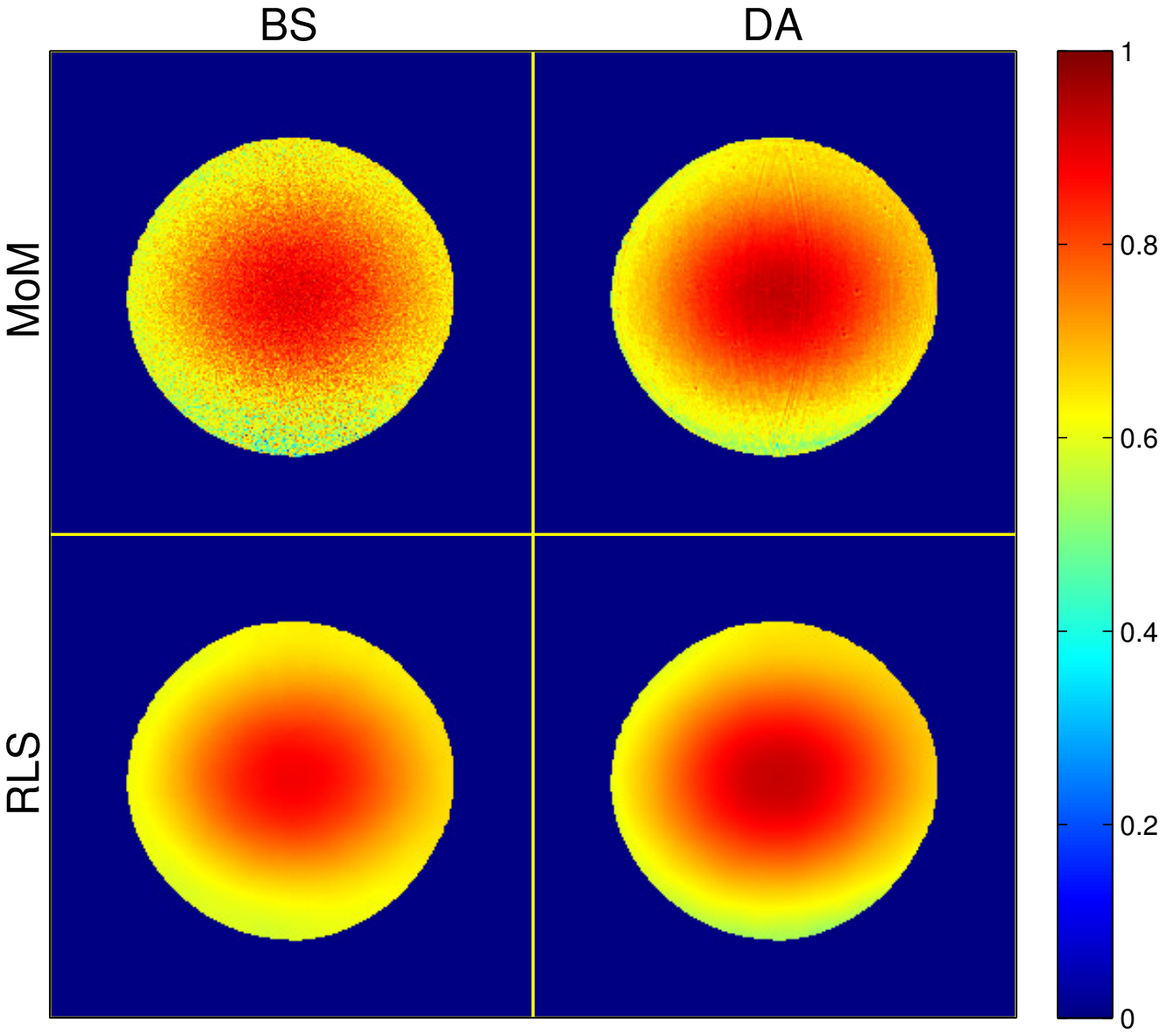

Figure S.5: Method of Moments (top) and RLS (bottom) estimates of flip angle scaling $\boldsymbol{\kappa}$ in a FIRST-BIRN gel phantom, from Bloch-Siegert (left) and Double-Angle (right) data. Well away from the phantom encasing, both estimates exhibit a paraboloidal spatial profile, but differ in scaling by $4.8 \pm 0.71\%$.

experiments. Unless explicitly mentioned in Section IV.C, these details pertain to brain reconstructions as well. Sections S.V.C and S.V.D discuss additional phantom and *in vivo* images and tables; in addition, Section S.V.D provides image registration details.

S.V.A SPGR/DESS (Phantom) Reconstructions

We acquire all phantom datasets using a GE Discovery™ MR750 3.0T scanner with an 8-channel receive head array. We separately normalize and combine coil data from each scan profile using a natural extension of [16] to the case of multiple datasets. For each optimized SPGR/DESS scan profile $\mathbf{P}^*$, we pre-cluster known parameter maps $\mathbf{N}$ into 10 clusters using k-means++ [19] and use each of the 10 cluster means to compute a corresponding dictionary of signal vectors from 300 T_1 and T_2 values logarithmically spaced between $[10^{1.5}, 10^{3.5}]$ and $[10^{0.5}, 10^{3}]$, respectively. We then iterate over clusters and use each dictionary in conjunction with corresponding coil-combined magnitude image data to produce ML parameter estimates $\widehat{\mathbf{X}}_{\mathrm{ML}}(\mathbf{N}, \mathbf{P}^*)$. We subsequently solve RLS problem (S.2) with initialization $\widehat{\mathbf{X}}_{\mathrm{ML}}(\mathbf{N}, \mathbf{P}^*)$ to obtain regularized estimates $\widehat{\mathbf{X}}_{\mathrm{RLS}}(\mathbf{N}, \mathbf{P}^*)$ for each $\mathbf{P}^*$. We design regularizers to encourage parameter estimates from different scan profiles to exhibit similar levels of smoothness. Letting $l \in \{1, 2, 3\}$ enumerate latent object parameters $\{\mathbf{M}_{0/\mathrm{E}}, \mathbf{T}_1, \mathbf{T}_2\}$, we choose mild regularization parameters $(\beta_1, \beta_2, \beta_3) := D \times (2^{-26}, 2^{-21}, 2^{-23})$ to scale with the number of datasets. For all scan profiles, we use a corner-rounded approximation to the ℓ_1 potential function,

$$\phi_l(\cdot) := \gamma_l^2 \left[\sqrt{1 + |\cdot/\gamma_l|^2} - 1 \right] \tag{S.5}$$

where $(\gamma_1, \gamma_2, \gamma_3) := (2^{-2}, 2^5 \text{ ms}, 2^2 \text{ ms})$ are fixed to values on the order of anticipated standard deviations. We iteratively update $\mathbf{X}$ until convergence criterion

$$\left\| \mathbf{X}^{(n)} - \mathbf{X}^{(n-1)} \right\|_F < 10^{-7} \left\| \mathbf{X}^{(n)} \right\|_F \tag{S.6}$$

is satisfied. For all steady-state profiles tested, ML initializations and RLS reconstructions of phantom datasets require less than 3m30s and 9s, respectively.

S.V.B IR/SE (Phantom) Reconstructions

We first jointly coil-combine all 8-channel IR and SE phantom datasets to produce complex images. We next estimate $\mathbf{T}_1$ along with nuisance parameters $\mathbf{M}_0 \exp(-T_{\mathrm{E}}/\mathbf{T}_2)$ and inversion efficiency map $\boldsymbol{\epsilon}$ via (S.1) and (S.3) from the 4 complex coil-combined IR images. By using the same flip angle scaling map $\widehat{\boldsymbol{\kappa}}$ as is used for SPGR/DESS profiles, we estimate $\mathbf{T}_1$ using a signal model similar to one proposed in [20], which accounts for imperfect excitation/refocusing and imperfect inversion. We then take both $\mathbf{T}_1$ and $\boldsymbol{\kappa}$ as known and estimate $\mathbf{T}_2$ along with nuisance parameter $\mathbf{M}_0$ (accounting for imperfect excitation/refocusing and incomplete recovery) via (S.1) and (S.3) from the 4 complex coil-combined SE images. We hold all other reconstruction details identical to those of SPGR/DESS reconstructions. For all steady-state scan profiles tested, ML initializations and RLS reconstructions of brain datasets require less than 3m and 7s, respectively.

As an aside: we initially attempted to circumvent sequential $\mathbf{T}_1$, then $\mathbf{T}_2$ estimation by instead jointly estimating $\mathbf{M}_0$, $\mathbf{T}_1$, $\mathbf{T}_2$, and $\boldsymbol{\epsilon}$ from the IR and SE datasets together. Even using magnitude data and signal models, this resulted in heavily biased parameter maps, possibly due to the dependence of adiabatic inversion efficiency on relaxation parameters [21].

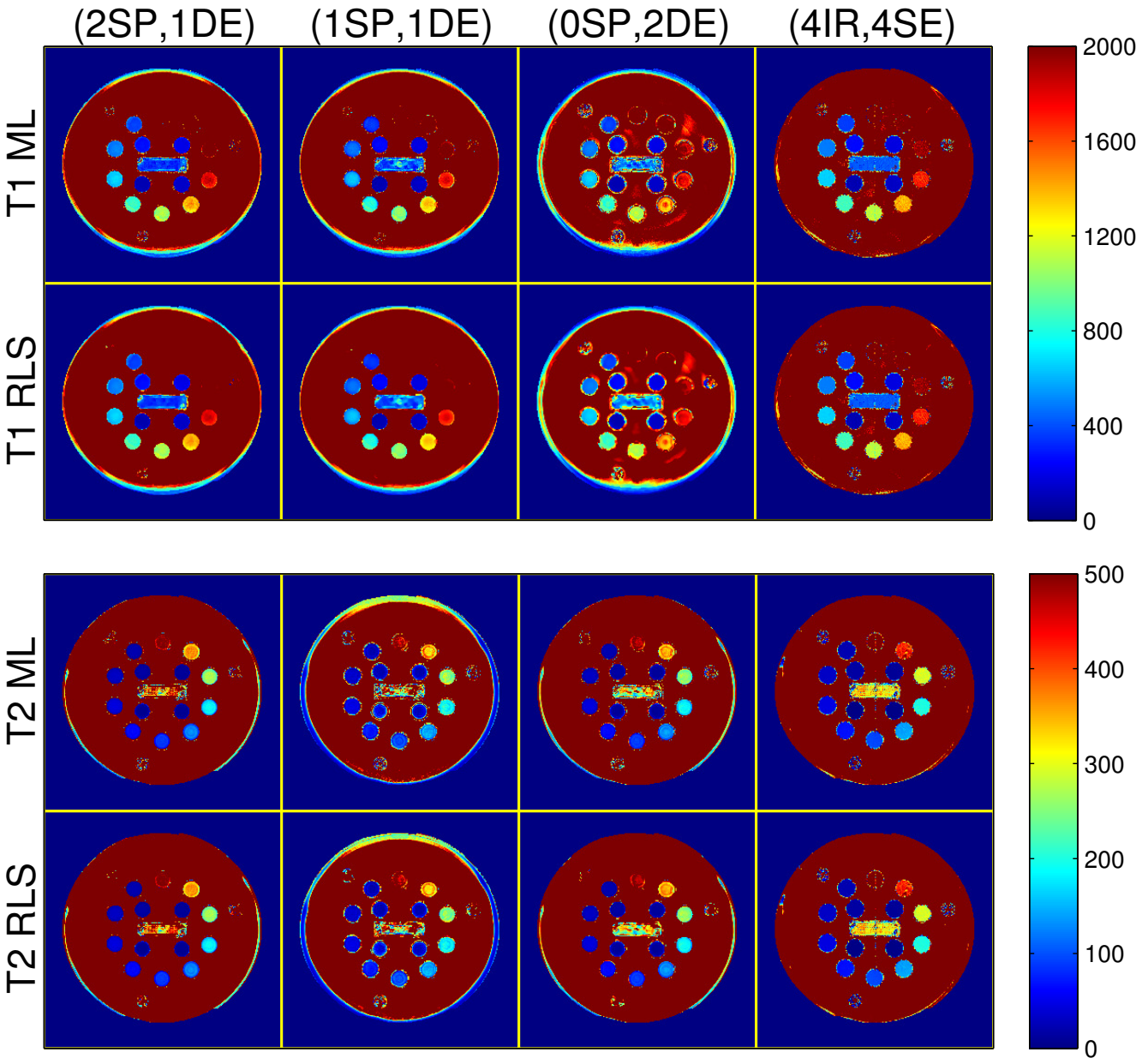

Figure S.6: Colorized $\mathbf{T}_1$ and $\mathbf{T}_2$ ML and RLS estimates from an HPD® quantitative phantom. Columns correspond to scan profiles consisting of (2 SPGR, 1 DESS), (1 SPGR, 1 DESS), (0 SPGR, 2 DESS), and (4 IR, 4 SE) acquisitions. Rows distinguish $\mathbf{T}_1$ and $\mathbf{T}_2$ ML and RLS estimators. Fig. S.7 provides identical grayscale images which enumerate vials. Colorbar ranges are in milliseconds.

S.V.C Phantom Images and Tables

Figs. S.6 and S.7 compare phantom $\mathbf{T}_1$ and $\mathbf{T}_2$ ML and RLS estimates in color and grayscale from optimized scan profiles. Vials are enumerated in Fig. S.7 in descending T_1 and T_2 order. Vials corresponding to tight $\mathcal{X}_\mathrm{t}$ and broad $\mathcal{X}_\mathrm{b}$ parameter ranges are highlighted with orange and yellow labels, respectively. Within these vials of interest, parameter maps from different scans appear visually similar.

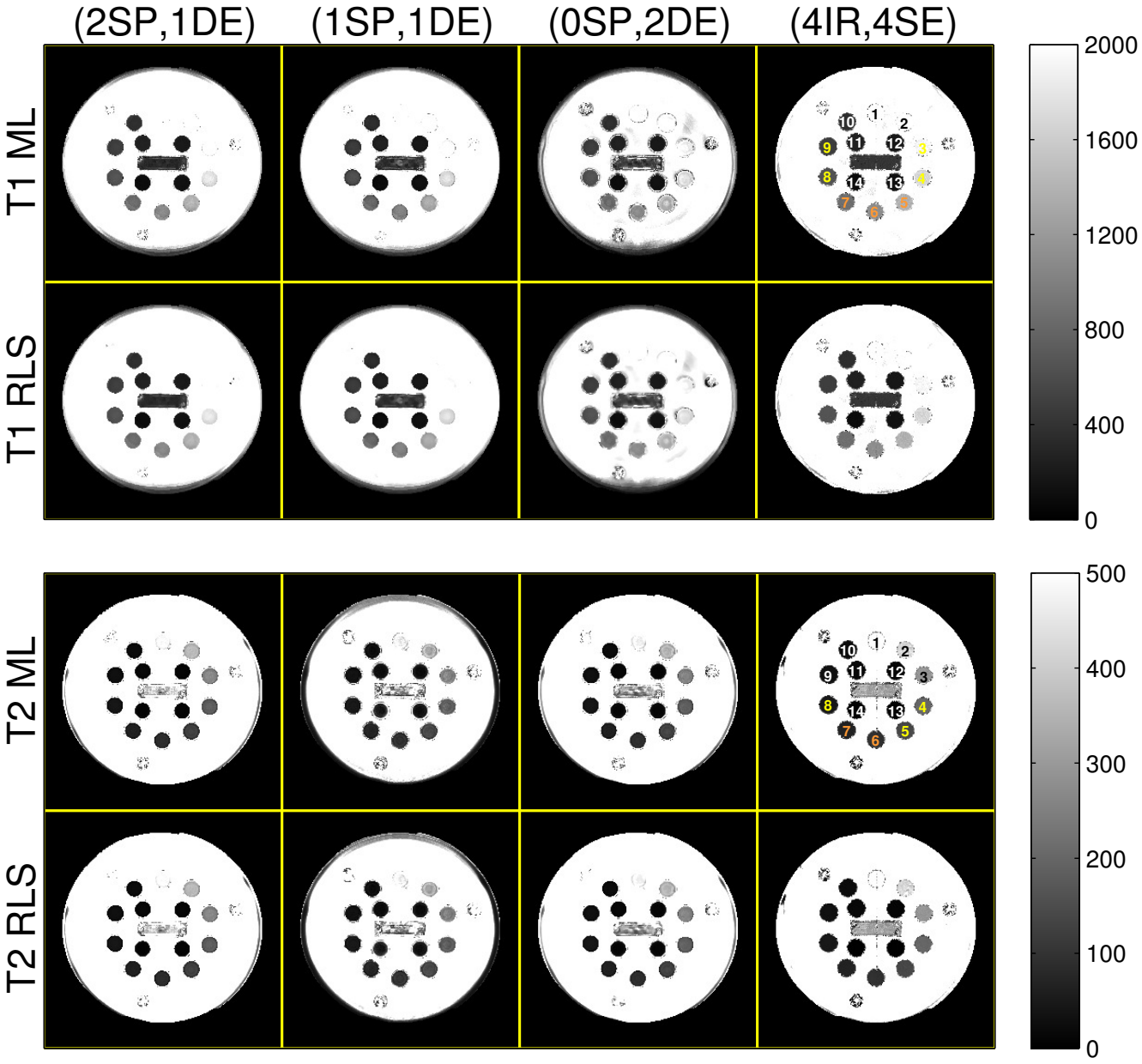

Figure S.7: Grayscale $\mathbf{T}_1$ and $\mathbf{T}_2$ ML and RLS estimates from an HPD® quantitative phantom. Columns correspond to scan profiles consisting of (2 SPGR, 1 DESS), (1 SPGR, 1 DESS), (0 SPGR, 2 DESS), and (4 IR, 4 SE) acquisitions. Rows distinguish $\mathbf{T}_1$ and $\mathbf{T}_2$ ML and RLS estimators. Vials are enumerated and color-coded to correspond with data points in Fig. S.8. Fig. S.6 provides identical colorized images. Colorbar ranges are in milliseconds.

In higher-T_1 vials (and the surrounding water), more bias is apparent in $\widehat{\mathbf{T}}_1$ ML and RLS estimates from the $(0, 2)$ scan profile than from the $(2, 1)$ and $(1, 1)$ scan profiles. With the signal models used in this study, the images suggest that scan profiles consisting of at least one SPGR scan may offer increased protection against T_1 estimation bias.

Fig. S.8 expands Fig. 1 by plotting phantom within-ROI sample statistics of both ML and RLS $\mathbf{T}_1, \mathbf{T}_2$ estimates. Table S.2 replicates sample statistics in Fig. S.8 for vials 5-8. Compared to ML initializations,

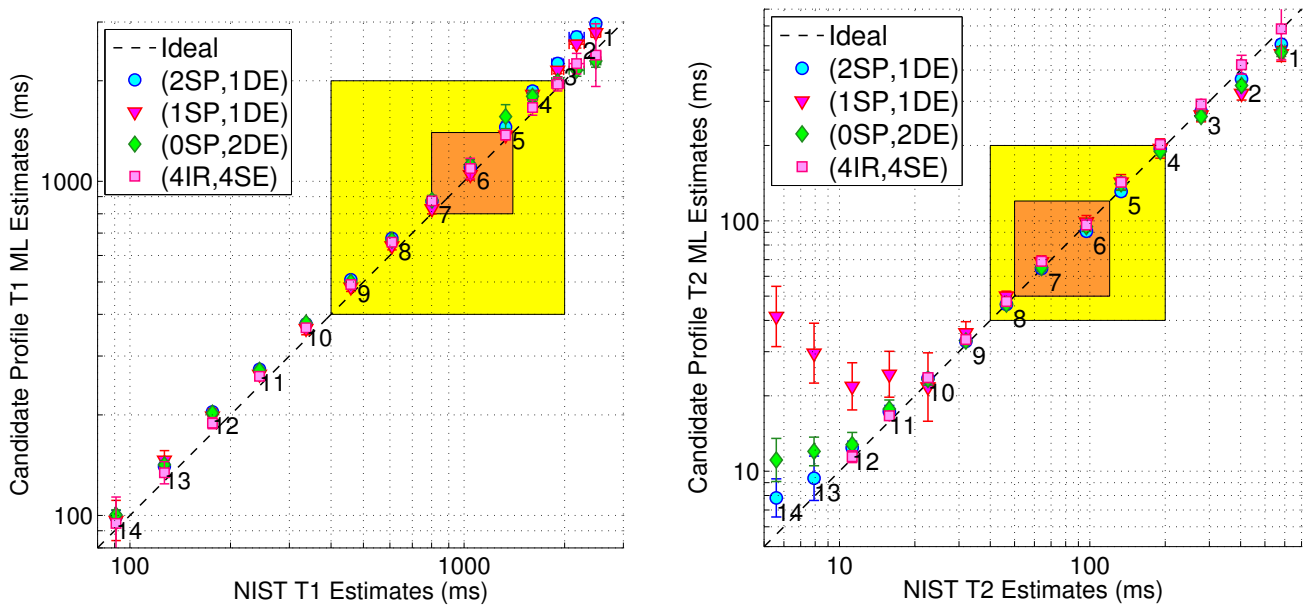

(a) $\widehat{T}_1^{\mathrm{ML}}$ Estimates

(b) $\widehat{T}_2^{\mathrm{ML}}$ Estimates

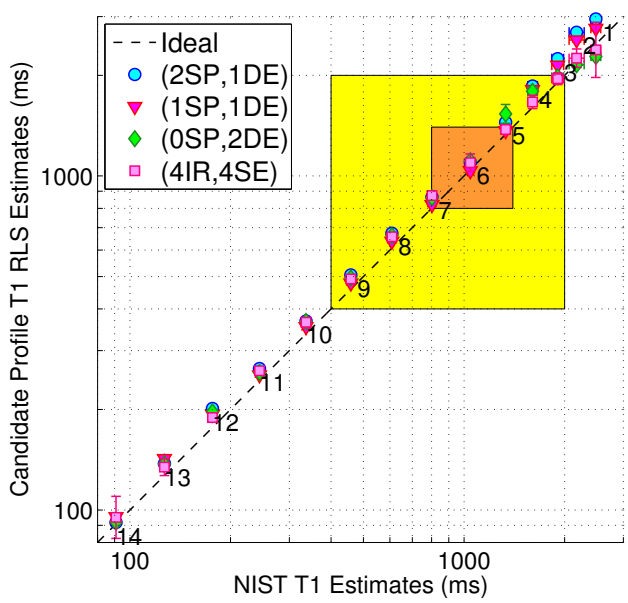

(c) $\widehat{T}_1^{\mathrm{RLS}}$ Estimates

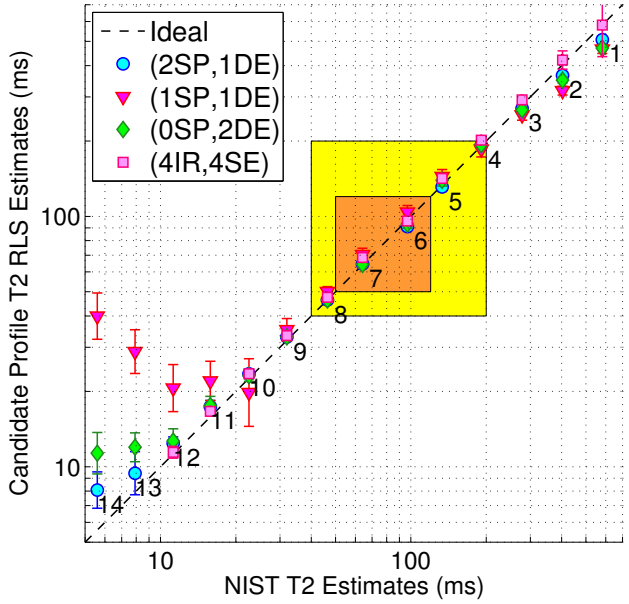

(d) $\widehat{T}_2^{\mathrm{RLS}}$ Estimates

Figure S.8: Phantom within-ROI sample statistics of $\mathbf{T}_1$ and $\mathbf{T}_2$ estimates from optimized SPGR/DESS and reference IR/SE scan profiles, vs. NIST NMR measurements [22]. Markers and error bars indicate ROI sample means and ROI sample standard deviations within the 14 labeled and color-coded vials in Fig. S.7. Figs. S.8a-S.8b correspond with ML estimates and replicate Figs. 1a-1b for sake of comparison. Figs. S.8c-S.8d correspond with RLS estimates. Tight $\mathcal{X}_{\mathrm{t}}$ and broad $\mathcal{X}_{\mathrm{b}}$ latent parameter ranges are highlighted in orange and yellow, respectively. Table S.2 replicates sample statistics within Vials 5-8. Our MR measurements are at 293K, while NIST NMR measurements are at 293.00K. Within the designed parameter ranges, estimates from different acquisitions are in reasonable agreement with NIST measurements.

	(2SP,1DE)	(1SP,1DE)	(0SP,2DE)	(4IR,4SE)	NIST NMR
V5 $\widehat{T}_1^{\mathrm{ML}}$	$1450 \pm 50.$	1380 ± 41	1600 ± 130	1380 ± 44	1332 ± 0.8
V5 $\widehat{T}_1^{\mathrm{RLS}}$	1450 ± 26	1370 ± 16	1540 ± 98	1380 ± 37	
V6 $\widehat{T}_1^{\mathrm{ML}}$	$1100 \pm 30.$	1050 ± 39	1120 ± 39	1100 ± 74	1044 ± 3.2
V6 $\widehat{T}_1^{\mathrm{RLS}}$	1100 ± 15	1040 ± 14	1110 ± 16	1100 ± 64	
V7 $\widehat{T}_1^{\mathrm{ML}}$	870 ± 22	830 ± 29	880 ± 29	870 ± 25	801.7 ± 1.70
V7 $\widehat{T}_1^{\mathrm{RLS}}$	865 ± 7.1	820 ± 11	860 ± 18	870 ± 21	
V8 $\widehat{T}_1^{\mathrm{ML}}$	680 ± 12	640 ± 18	670 ± 12	658 ± 8.8	608.6 ± 1.03
V8 $\widehat{T}_1^{\mathrm{RLS}}$	674 ± 7.6	637 ± 7.4	662 ± 6.6	658 ± 7.1	
V5 $\widehat{T}_2^{\mathrm{ML}}$	131 ± 5.5	$140 \pm 10.$	141 ± 8.4	143 ± 4.9	133.27 ± 0.073
V5 $\widehat{T}_2^{\mathrm{RLS}}$	131 ± 5.2	145 ± 9.1	139 ± 7.1	142 ± 4.8	
V6 $\widehat{T}_2^{\mathrm{ML}}$	91 ± 3.5	99 ± 6.0	95 ± 4.2	96 ± 2.7	96.89 ± 0.049
V6 $\widehat{T}_2^{\mathrm{RLS}}$	91 ± 3.4	104 ± 6.2	93 ± 3.7	96 ± 2.6	
V7 $\widehat{T}_2^{\mathrm{ML}}$	64 ± 2.2	69 ± 3.9	65 ± 2.1	69 ± 1.2	64.07 ± 0.034
V7 $\widehat{T}_2^{\mathrm{RLS}}$	65 ± 2.1	71 ± 4.3	64 ± 1.9	69 ± 1.2	
V8 $\widehat{T}_2^{\mathrm{ML}}$	46 ± 1.5	$50. \pm 2.3$	46 ± 1.1	47.6 ± 0.87	46.42 ± 0.014
V8 $\widehat{T}_2^{\mathrm{RLS}}$	46 ± 1.5	$50. \pm 2.3$	46 ± 1.0	47.5 ± 0.85	

Table S.2: Phantom within-ROI sample means $\pm$ sample standard deviations of $\mathbf{T}_1$ and $\mathbf{T}_2$ estimates from optimized SPGR/DESS and reference IR/SE scan profiles, vs. NIST NMR measurements (*cf.* slide 22 of e-poster corresponding to [22]). For sake of brevity, sample statistics corresponding only to phantom vials within (or nearly within) tight design range $\mathcal{X}_{\mathrm{t}}$ (color-coded orange in Fig. S.7) are reported. Fig. S.8 plots sample statistics for all vials. 'V#' abbreviates vial numbers. All values are reported in milliseconds.

(weakly) regularized estimates reduce error bars without introducing substantial additional bias.

S.V.D Brain Registration Details, Images, and Tables

For each coil-combined dataset, we compute a separate 2D rigid transformation (with respect to the $T_{\mathrm{I}} = 50$ms IR dataset) via the MATLAB® function `imregtform` and then apply the transformation via `imwarp`. We choose to use rigid transformations instead of affine distortions to avoid scaling; however in doing so we sacrifice compensating for small through-plane rotations. We do not find registration to substantially change subsequently estimated relaxation maps; however, this extra step substantially improves alignment of (especially cortical GM) ROIs in $\widehat{T}_1$ and $\widehat{T}_2$ estimates from different scan profiles.

Fig. S.9 expands Fig. 2 by comparing both ML and RLS $\mathbf{T}_1, \mathbf{T}_2$ estimates across scan profiles. Fig. S.10 replicates Fig. S.9 in grayscale. Table S.3 is similar to Table IV, except for RLS estimates. Compared to ML counterparts, RLS estimates in general reduce within-ROI sample variation without incurring significant additional bias.

S.VI Multi-exponential Relaxation

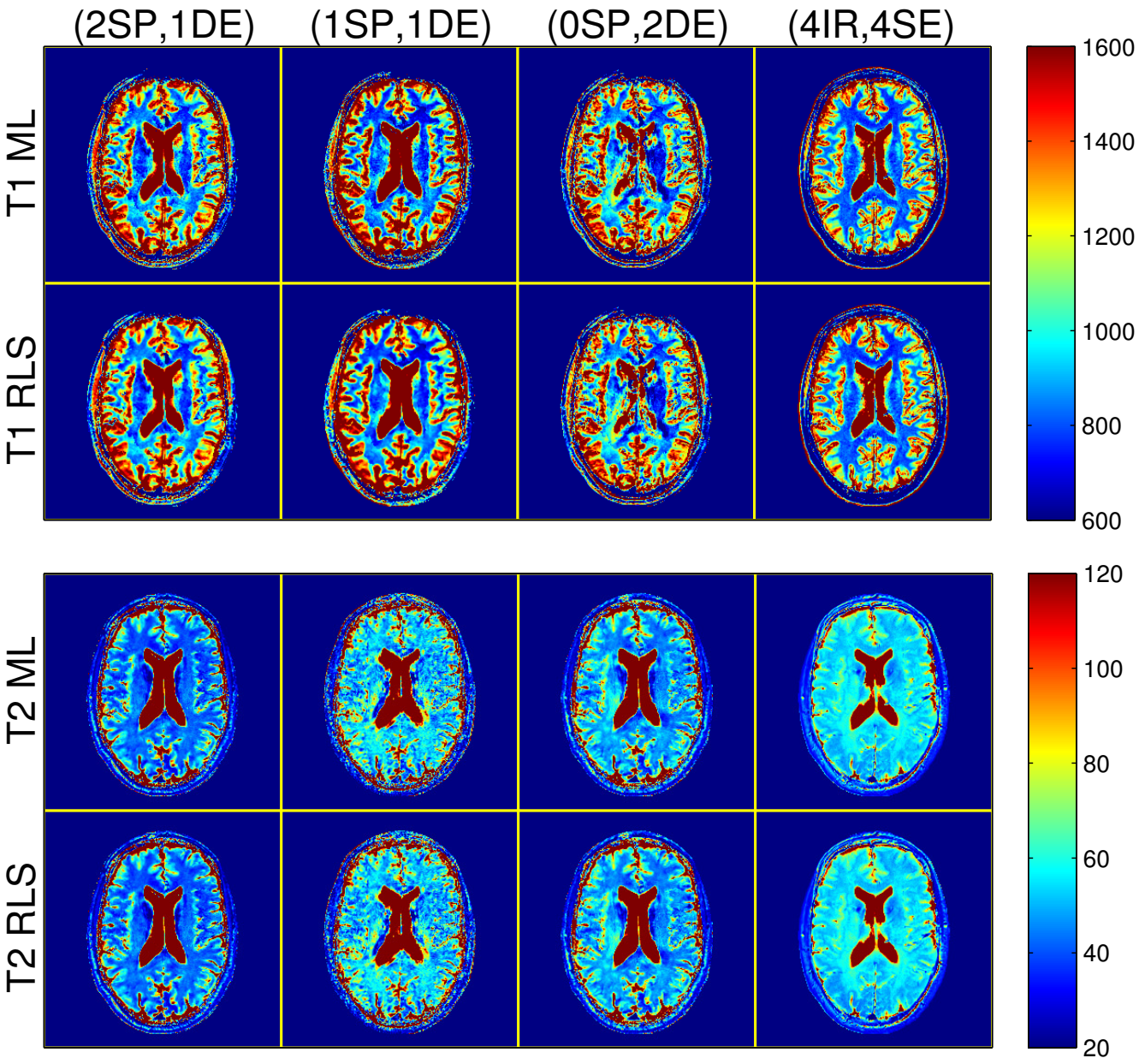

Figure S.9: Grayscale $\mathbf{T}_1$ and $\mathbf{T}_2$ ML and RLS estimates from the brain of a healthy volunteer. Columns correspond to profiles consisting of (2 SPGR, 1 DESS), (1 SPGR, 1 DESS), (0 SPGR, 2 DESS), and (4 IR, 4 SE) acquisitions. Rows distinguish $\mathbf{T}_1$ and $\mathbf{T}_2$ ML and RLS estimators. Fig. S.10 provides identical grayscale images. Colorbar ranges are in milliseconds.

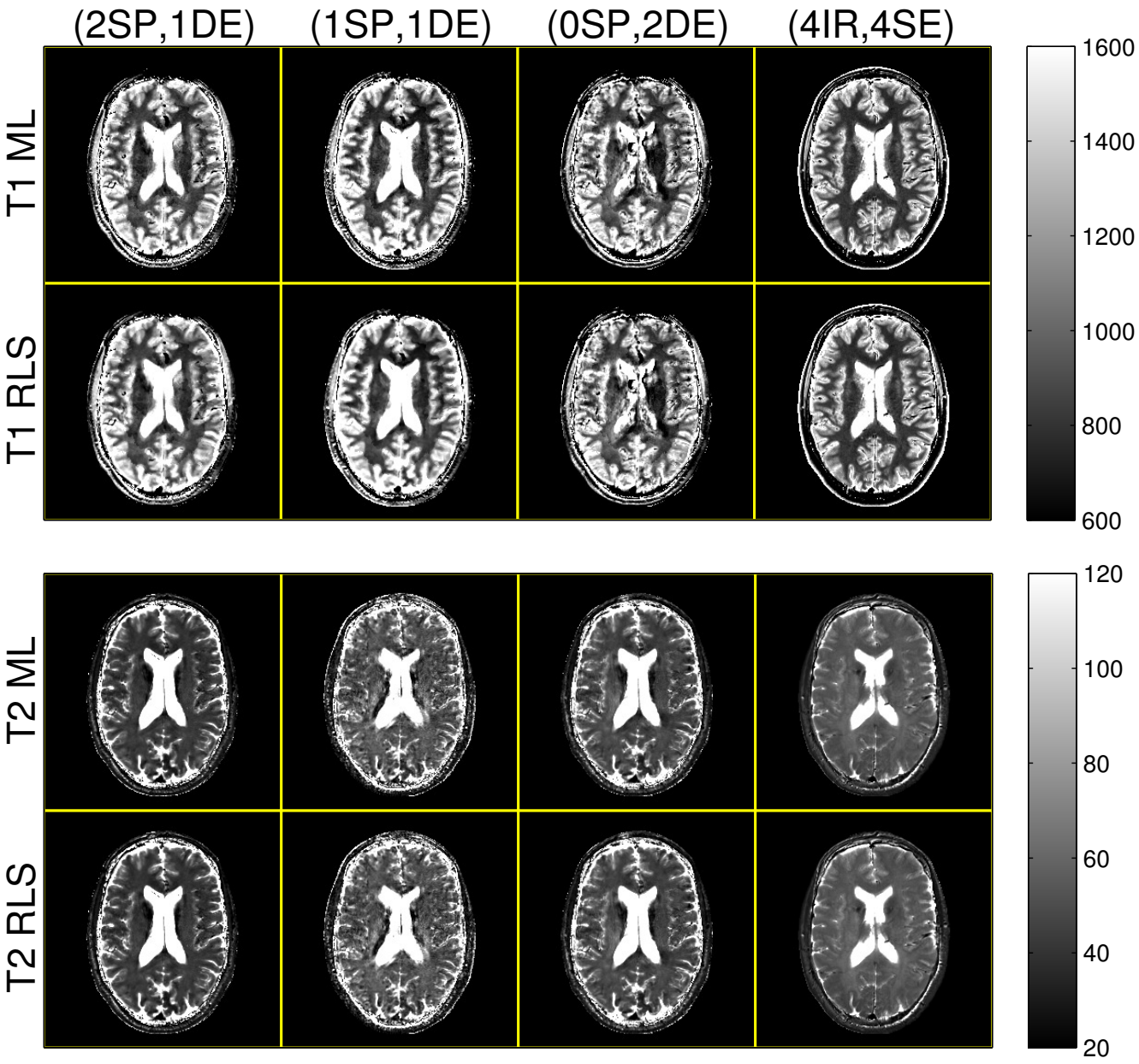

Figure S.10: Grayscale $\mathbf{T}_1$ and $\mathbf{T}_2$ ML and RLS estimates from the brain of a healthy volunteer. Columns correspond to profiles consisting of (2 SPGR, 1 DESS), (1 SPGR, 1 DESS), (0 SPGR, 2 DESS), and (4 IR, 4 SE) acquisitions. Rows distinguish $\mathbf{T}_1$ and $\mathbf{T}_2$ ML and RLS estimators. Fig. S.9 provides identical colorized images. Colorbar ranges are in milliseconds.

	ROI (color)	(2SP,1DE)	(1SP,1DE)	(0SP,2DE)	(4IR,4SE)
$\widehat{T}_1^{\mathrm{RLS}}$	anterior right WM (yellow)	840 ± 24	$770 \pm 20.$	840 ± 43	$780 \pm 20.$
	anterior left WM (magenta)	740 ± 51	670 ± 37	740 ± 54	760 ± 23
	posterior right WM (green)	890 ± 79	860 ± 61	960 ± 82	810 ± 24
	posterior left WM (blue)	870 ± 62	$850 \pm 50.$	880 ± 78	820 ± 35
	anterior GM (cyan)	1200 ± 200	1200 ± 220	1300 ± 230	1300 ± 180
$\widehat{T}_2^{\mathrm{RLS}}$	anterior right WM (yellow)	$40. \pm 1.3$	54 ± 3.4	46 ± 1.5	55 ± 1.9
	anterior left WM (magenta)	$40. \pm 1.7$	$50. \pm 4.4$	43 ± 1.7	53 ± 1.8
	posterior right WM (green)	43 ± 2.8	$60. \pm 6.7$	51 ± 3.7	58 ± 2.3
	posterior left WM (blue)	43 ± 1.7	57 ± 4.7	49 ± 2.5	57 ± 1.8
	anterior GM (cyan)	50 ± 12	60 ± 15	60 ± 11	59 ± 6.4

Table S.3: Within-ROI sample means $\pm$ within-ROI sample standard deviations of $\mathbf{T}_1$ and $\mathbf{T}_2$ RLS estimates from the brain of a healthy volunteer. Sample statistics are computed within ROIs indicated in Fig. 2. All values are reported in milliseconds.

	ROI (color)	$[10, 30]^{\mathsf{T}}$	$[10, 60]^{\mathsf{T}}$	$[10, 150]^{\mathsf{T}}$
$\widehat{T}_2^{\mathrm{ML}}$	anterior right WM (yellow)	54 ± 3.0	56 ± 1.9	54 ± 2.4
	anterior left WM (magenta)	$50. \pm 2.2$	54 ± 1.8	54 ± 2.4
	posterior right WM (green)	55 ± 2.6	58 ± 2.2	61 ± 2.6
	posterior left WM (blue)	50 ± 2.2	57 ± 2.0	61 ± 2.1
	anterior GM (cyan)	58 ± 6.5	61 ± 6.8	57 ± 7.3

Table S.4: Within-ROI sample means $\pm$ within-ROI sample standard deviations of monoexponential $\mathbf{T}_2$ ML estimates, from pairs of *in vivo* SE datasets. Column headers indicate echo times $\mathbf{T}_{\mathrm{E}}$ (ms) of SE datasets. Sample statistics are computed within ROIs indicated in Fig. 2. Single-component $\widehat{T}_2^{\mathrm{ML}}$ estimates in WM depend on SE echo times.

This section explores the effect of model mismatch due to multi-component relaxation on single-component $\mathbf{T}_2$ estimation bias, through numerical simulations and *in vivo* experiments.

We simulate multi-exponential data to arise from three non-exchanging pools of myelinated water $(T_1, T_2) \leftarrow (500, 20)$ms, intracellular and extracellular water $(T_1, T_2) \leftarrow (1000, 80)$ms, and free water $(T_1, T_2) \leftarrow (3500, 250)$ms [23, 24]. We assign pool fractions of $(0.15, 0.80, 0.05)$ in WM and $(0, 0.95, 0.05)$ in GM to the 81st slice of the BrainWeb digital phantom [25, 26] to create ground truth $\mathbf{M}_0$, $\mathbf{T}_1$, and $\mathbf{T}_2$ compartment-wise maps. We simulate component-wise IR signals (acquisition parameters in Section IV.B.1) and add them to yield noiseless multi-component IR data. We likewise simulate and then add component-wise SE signals to construct three scan profiles consisting of pairs of multi-component SE datasets with variable $\mathbf{T}_{\mathrm{E}} \in \left\{[10, 30]^{\mathsf{T}}, [10, 60]^{\mathsf{T}}, [10, 150]^{\mathsf{T}}\right\}$. To avoid confounding sources of bias, we assume knowledge of a uniform transmit field and a uniform sensitivity profile of a single-channel receive coil. We estimate a single-component $\widehat{\mathbf{T}}_1$ ML map from multi-component IR data, which we then use to estimate a single-component $\widehat{\mathbf{T}}_2$ ML map from each multi-exponential SE scan profile.

The upper rows of Figs. S.11 and S.12 compare (in color and grayscale) $\widehat{\mathbf{T}}_2$ maps from simulated multi-exponential SE data. The lower rows compare *in vivo* $\widehat{\mathbf{T}}_2$ maps from corresponding subsets of the SE reference profile discussed in Section IV.C. As echo times are further separated, $\widehat{T}_2$ in WM approaches $\widehat{T}_2$ in GM, creating an apparent reduction in $\widehat{T}_2$ WM/GM contrast.

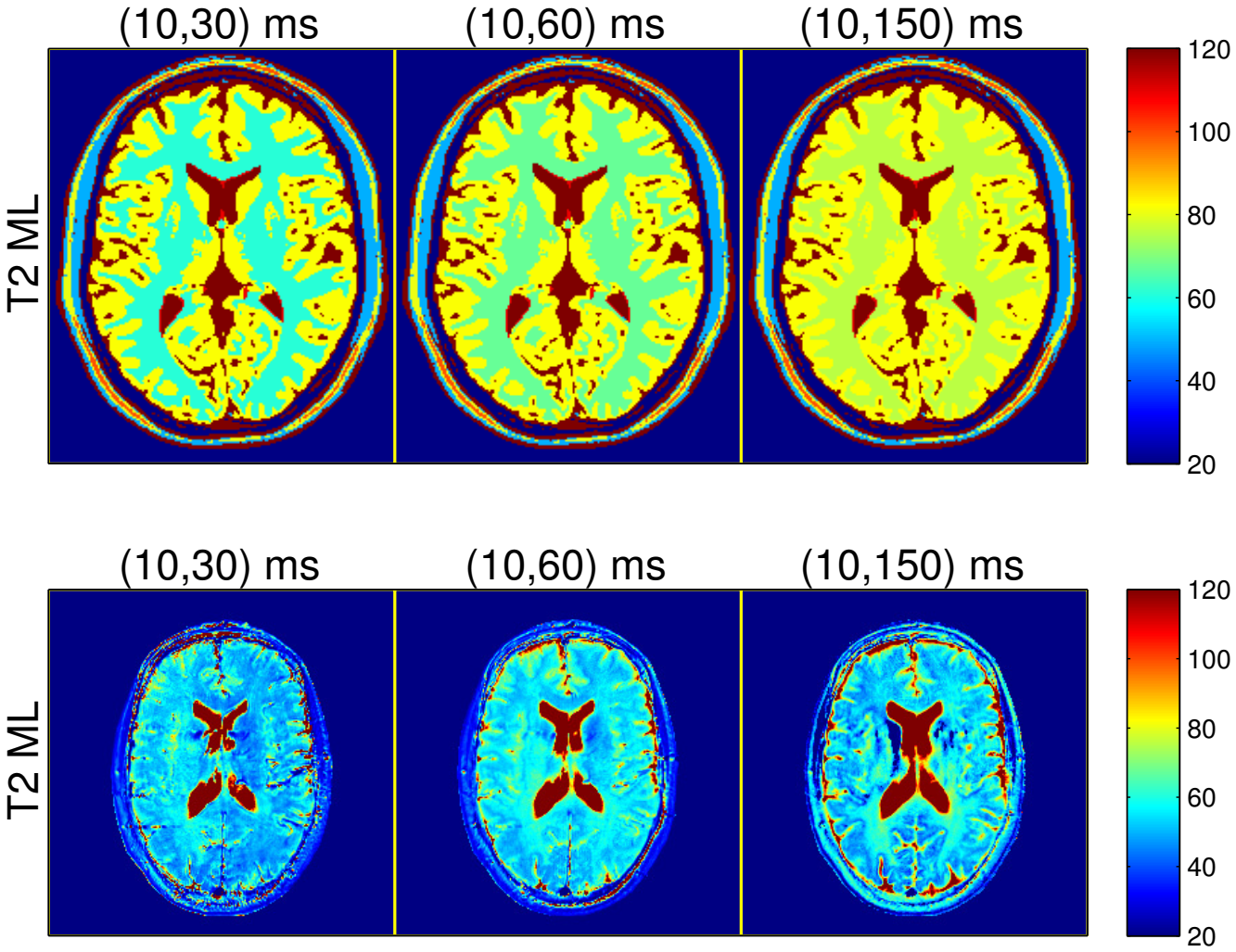

Figure S.11: Colorized monoexponential $\mathbf{T}_2$ ML estimates from pairs of (top) multi-exponential simulated and (bottom) *in vivo* SE datasets. Columns denote SE dataset echo times. Fig. S.12b provides identical grayscale images. Colorbar ranges are in milliseconds.

Table S.4 summarizes $\widehat{T}_2^{\mathrm{ML}}$ sample means and sample standard deviations (computed within WM/GM ROIs depicted in Fig. 2) from *in vivo* SE scan profiles. Single-component $\widehat{T}_2^{\mathrm{ML}}$ estimates depend on SE echo times more significantly in WM than in GM. Comparing with Table IV, trends suggest that disagreement in $\widehat{T}_2^{\mathrm{ML}}$ estimates across scan profiles may in part be attributable to the substantial differences of acquisition parameters (*e.g.* echo time) used in different pulse sequences.

References

[1] G. Nataraj, J.-F. Nielsen, and J. A. Fessler, "Optimizing MR scan design for model-based T1, T2 estimation from steady-state sequences," *IEEE Trans. Med. Imag.*, 2016, to appear.

[2] H. Z. Wang, S. J. Riederer, and J. N. Lee, "Optimizing the precision in T1 relaxation estimation using limited flip angles," *Mag. Res. Med.*, vol. 5, no. 5, pp. 399–416, Nov. 1987.

[3] L. Fleysher, R. Fleysher, S. Liu, W. Zaaraoui, and O. Gonen, "Optimizing the precision-per-unit-time of quantitative MR metrics: Examples for T_1, T_2, and DTI," *Mag. Res. Med.*, vol. 57, no. 2, pp. 380–7, Feb. 2007.

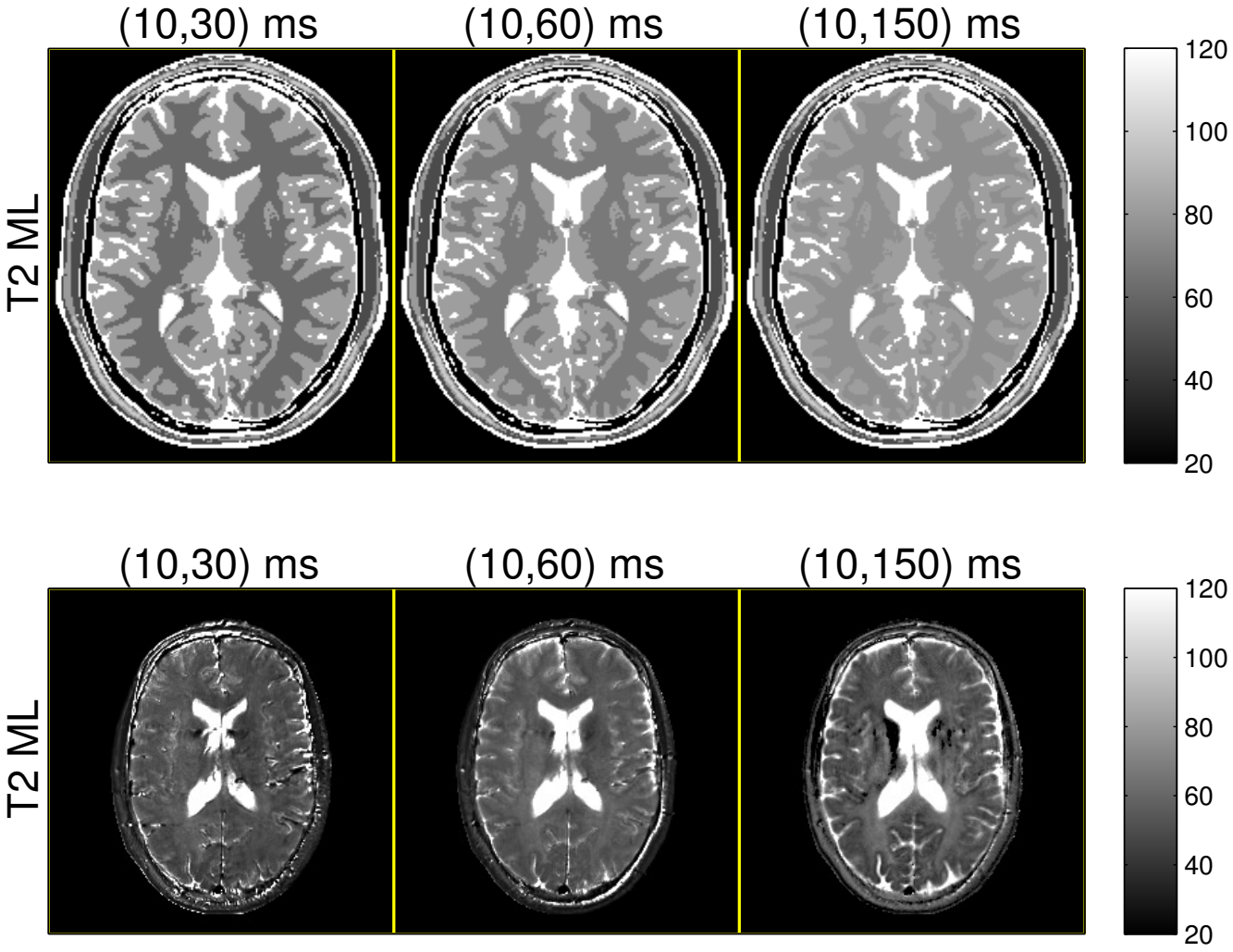

Figure S.12: Grayscale monoexponential $\mathbf{T}_2$ ML estimates from pairs of (top) multi-exponential simulated and (bottom) *in vivo* SE datasets. Columns denote SE dataset echo times. Fig. S.11b provides identical colorized images. Colorbar ranges are in milliseconds.

[4] J. Imran, François. Langevin, and Hervé. Saint-Jalmes, "Two-point method for T1 estimation with optimized gradient-echo sequence," *Mag. Res. Im.*, vol. 17, no. 9, pp. 1347–56, Nov. 1999.

[5] S. C. L. Deoni, B. K. Rutt, and T. M. Peters, "Rapid combined T1 and T2 mapping using gradient recalled acquisition in the steady state," *Mag. Res. Med.*, vol. 49, no. 3, pp. 515–26, Mar. 2003.

[6] S. C. L. Deoni, T. M. Peters, and B. K. Rutt, "Determination of optimal angles for variable nutation proton magnetic spin-lattice, T_1, and spin-spin, T_2, relaxation times measurement," *Mag. Res. Med.*, vol. 51, no. 1, pp. 194–9, Jan. 2004.

[7] C. Kanzow, N. Yamashita, and M. Fukushima, "Levenberg-Marquardt methods with strong local convergence properties for solving nonlinear equations with convex constraints," *J. Comp. Appl. Math.*, vol. 172, no. 2, pp. 375–97, Dec. 2004.

[8] G. Golub and V. Pereyra, "Separable nonlinear least squares: the variable projection method and its applications," *Inverse Prob.*, vol. 19, no. 2, pp. R1–26, Apr. 2003.

[9] S. G. Mallat and Z. Zhang, "Matching pursuits with time-frequency dictionaries," *IEEE Trans. Sig. Proc.*, vol. 41, no. 12, pp. 3397–415, Dec. 1993.

[10] J. P. Haldar, J. Anderson, and S. W. Sun, "Maximum likelihood estimation of T1 relaxation parameters using VARPRO," in *Proc. Intl. Soc. Mag. Res. Med.*, 2007, p. 41. [Online]. Available: http://cds.ismrm.org/ismrm-2007/files/00041.pdf

[11] J. A. Fessler, "Mean and variance of implicitly defined biased estimators (such as penalized maximum likelihood): Applications to tomography," *IEEE Trans. Im. Proc.*, vol. 5, no. 3, pp. 493–506, Mar. 1996.

[12] H. Gudbjartsson and S. Patz, "The Rician distribution of noisy MRI data," *Mag. Res. Med.*, vol. 34, no. 6, pp. 910–4, Dec. 1995.
[13] L. I. Sacolick, F. Wiesinger, I. Hancu, and M. W. Vogel, "B1 mapping by Bloch-Siegert shift," *Mag. Res. Med.*, vol. 63, no. 5, pp. 1315–22, May 2010.
[14] E. K. Insko and L. Bolinger, "Mapping of the radiofrequency field," *J. Mag. Res. A*, vol. 103, no. 1, pp. 82–5, Jun. 1993.
[15] L. Friedman and G. H. Glover, "Report on a multicenter fMRI quality assurance protocol," *J. Mag. Res. Im.*, vol. 23, no. 6, pp. 827–39, Jun. 2006.
[16] L. Ying and J. Sheng, "Joint image reconstruction and sensitivity estimation in SENSE (JSENSE)," *Mag. Res. Med.*, vol. 57, no. 6, pp. 1196–1202, Jun. 2007.
[17] H. Sun, W. A. Grissom, and J. A. Fessler, "Regularized estimation of Bloch-Siegert B1+ Maps in MRI," in *Proc. IEEE Intl. Conf. on Image Processing*, 2014, pp. 3646–50.
[18] A. Funai, J. A. Fessler, W. Grissom, and D. C. Noll, "Regularized B1+ map estimation in MRI," in *Proc. IEEE Intl. Symp. Biomed. Imag.*, 2007, pp. 616–9.
[19] D. Arthur and S. Vassilvitskii, "K-means++: The advantages of careful seeding," in *Proc. 18th Annual ACM-SIAM Symp. Disc. Alg. (SODA)*, 2007, pp. 1027–35. [Online]. Available: http://dl.acm.org/citation.cfm?id=1283494
[20] J. K. Barral, E. Gudmundson, N. Stikov, M. Etezadi-Amoli, P. Stoica, and D. G. Nishimura, "A robust methodology for in vivo T1 mapping," *Mag. Res. Med.*, vol. 64, no. 4, pp. 1057–67, Oct. 2010.
[21] L. R. Frank, E. C. Wong, and R. B. Buxton, "Slice profile effects in adiabatic inversion: Application to multislice perfusion imaging," *Mag. Res. Med.*, vol. 38, no. 4, pp. 558–64, Oct. 1997.
[22] K. E. Keenan, K. F. Stupic, M. A. Boss, S. E. Russek, T. L. Chenevert, P. V. Prasad, W. E. Reddick, K. M. Cecil, J. Zheng, P. Hu, and E. F. Jackson, "Multi-site, multi-vendor comparison of T1 measurement using ISMRM/NIST system phantom," in *Proc. Intl. Soc. Mag. Res. Med.*, 2016, p. 3290.
[23] A. Mackay, K. Whittall, J. Adler, D. Li, D. Paty, and D. Graeb, "In vivo visualization of myelin water in brain by magnetic resonance," *Mag. Res. Med.*, vol. 31, no. 6, pp. 673–7, Jun. 1994.
[24] S. C. L. Deoni, L. Matthews, and S. H. Kolind, "One component? Two components? Three? The effect of including a nonexchanging "free" water component in multicomponent driven equilibrium single pulse observation of T1 and T2," *Mag. Res. Med.*, vol. 70, no. 1, pp. 147–54, Jul. 2013.
[25] R. K.-S. Kwan, A. C. Evans, and G. B. Pike, "MRI simulation-based evaluation of image-processing and classification methods," *IEEE Trans. Med. Imag.*, vol. 18, no. 11, pp. 1085–97, Nov. 1999.
[26] D. L. Collins, A. P. Zijdenbos, V. Kollokian, J. G. Sled, N. J. Kabani, C. J. Holmes, and A. C. Evans, "Design and construction of a realistic digital brain phantom," *IEEE Trans. Med. Imag.*, vol. 17, no. 3, pp. 463–8, Jun. 1998.